

Linear Viscoelastic Properties of the Vertex Model for Epithelial Tissues

Sijie Tong,¹ Navreeta K. Singh,¹ Rastko Sknepnek,^{2,3,*} and Andrej Košmrlj^{1,4,†}

¹*Department of Mechanical and Aerospace Engineering,
Princeton University, Princeton, New Jersey 08544, USA*

²*School of Science and Engineering, University of Dundee, Dundee DD1 4HN, United Kingdom*

³*School of Life Sciences, University of Dundee, Dundee DD1 5EH, United Kingdom*

⁴*Princeton Institute for the Science and Technology of Materials (PRISM),
Princeton University, Princeton, New Jersey 08544, USA*

Epithelial tissues act as barriers and, therefore, must repair themselves, respond to environmental changes and grow without compromising their integrity. Consequently, they exhibit complex viscoelastic rheological behavior where constituent cells actively tune their mechanical properties to change the overall response of the tissue, e.g., from fluid-like to solid-like. Mesoscopic mechanical properties of epithelia are commonly modeled with the vertex model (VM). We systematically studied rheological properties of the VM by applying small oscillatory shear and bulk deformations and measuring the response stresses. We found that the shear and bulk responses in the fluid and solid phases can be described by standard spring-dashpot viscoelastic models. Further, we found that the solid-fluid transition can be tuned by applying pre-deformation to the system. Thus, the VM's rich rheological behavior makes it suitable for describing mesoscale dynamics of epithelial tissues beyond the quasistatic limit.

INTRODUCTION

The development and maintenance of tissues requires close coordination of biochemical and mechanical signaling [1–3]. There is, for instance, mounting evidence for the key role played by tissue material properties and their regulation during embryonic development [4]. Tissues must be able to adjust their mechanical properties in response to internal and external stimuli. In particular, epithelial tissues, which line all cavities in the body and demarcate organs, must sustain substantial mechanical stresses while also supporting numerous biological processes such as selective diffusion and absorption/secretion [5]. In homeostasis, the tissue must maintain its shape and resist deformation while remaining flexible. The tissue must also be able to regenerate and repair itself, often with fast turnover, e.g., in gut epithelia [6]. Furthermore, in morphogenesis, the tissue must take up a specific shape and function [7]. During metastasis, however, the shape is lost and cancer cells invade surrounding healthy tissue [8]. All of these processes require that cells be able to move, often over distances much larger than the cell size. During cell migration, however, the tissue must maintain its integrity. It is, therefore, not surprising that tissues exhibit rich viscoelastic behavior [9]. Unlike passive viscoelastic materials, a tissue can actively tune its rheological response, making the study of its rheology not only important for understanding biological functions but also an interesting problem from the perspective of the physics of active matter systems [10].

Collective cell migration has been extensively studied in biology [11] and biophysics [12]. In vitro studies of

confluent cell monolayers [13–17] focused on the physical aspects of force generation and transmission and showed that cell migration is an inherently collective phenomenon. Some aspects of collective cell migration are remarkably similar to slow dynamics of structural glasses [18–24]. This suggests that many of the observed behaviors share common underlying mechanisms and can be understood, at least at mesoscales (i.e., distances beyond several cell diameters), using physics of dense active systems [25]. A particularly intriguing observation is that tuning cell density [18, 26, 27], strength of cell-cell and cell-substrate interactions [28], or cell shape parameters [21, 29] can cause the collective migration to stop. In other words, the tissue undergoes fluid to solid transition. Signatures of such behavior have been reported in several in vitro [19, 30] and developmental systems [31–33]. This suggests that important aspects of morphogenetic development might rely on tissue's ability to undergo phase transitions [4].

How a tissue responds to external and internal mechanical stresses will depend on its rheological (i.e., material) properties. While there have been numerous studies focusing on the rheology of a single cell [34–36], much less is known about tissue rheology, particularly during development. In order to develop a comprehensive understanding of tissue mechanics, such insight is key. Though single cell measurements are valuable, the mechanics of a tissue can be drastically different from that of its constituent cells. The stiffness of cell monolayers, for example, is orders of magnitude higher than the stiffness of constituent cells, while the time dependent mechanical behaviors of monolayers in response to deformation vary depending on the magnitude of loading [37]. Embryonic cell aggregates have been shown to behave elastically (i.e., solid-like) at short time scales but flow like fluids at long time scales, which facilitates both the robustness needed to maintain integrity and the flexibil-

* r.sknepnek@dundee.ac.uk

† andrej@princeton.edu

ity to morph during development [9]. Experiments have characterized the mechanical behaviors of tissues at various loading conditions, which led to a phenomenological description that models the relaxation properties of epithelial monolayers based on fractional calculus [38]. Notably, a recent particle-based model that includes cell division and apoptosis provided a plausible microscopic model for nonlinear rheological response [39]. Particle-based models are, however, unable to capture geometric aspects such as cell shape. It is, therefore, necessary to investigate rheological response in geometric models.

The vertex model (VM) [40–42] and more recent, closely related self-propelled Voronoi models (SPV) [21, 43] have played an important role in modeling mechanics of epithelial tissues since they account for the shapes of individual cells and provide a link to cellular processes, such as cell-cell adhesion, cell motility, and mitosis [42]. These geometric models are also able to capture the solid to fluid transition and demonstrate rich and unusual nonlinear mechanical behavior [44, 45]. While the mechanical properties of the VM and SPV have been extensively studied, most works to date focused on the long-time behavior, e.g., by studying the quasistatic shear modulus [20], effective diffusion constant of cells that is related to the viscosity of tissues [21], and correlations between a structural property called “softness” and the likelihood of topological rearrangements of cells [46]. The rheological properties of the VM that cover a broad range of time scales, however, have not yet been systematically explored. In this paper, we present a detailed study of the rheology of the VM by studying its response to applied oscillatory shear and bulk deformations of small amplitude, i.e., in the linear response regime. We measured the response stresses and used them to compute the storage and loss moduli in both the solid and fluid phases. We show that the dynamical response of the VM can be fitted to standard spring-dashpot viscoelastic models over seven decades in the driving frequency and that the solid-fluid transition can be tuned by applying pre-deformation to the system. Thus we argue that the VM makes a suitable basis for studies of tissue dynamics beyond the quasistatic limit.

RESULTS

Vertex model dynamics. In the VM, the state of an epithelial tissue is approximated as a polygonal tiling of the plane. The degrees of freedom are vertices, i.e., meeting points of three or more cell-cell junctions. In the simplest formulation, junctions are assumed to be straight lines. The energy of the VM is a quadratic function of cell areas and perimeters [41], i.e.,

$$E = \sum_C \left[\frac{K_C}{2} (A_C - A_{C0})^2 + \frac{\Gamma_C}{2} (P_C - P_{C0})^2 \right], \quad (1)$$

where K_C and Γ_C are the area and perimeter elastic moduli. A_C and A_{C0} are the actual and preferred areas of cell

C , respectively. Similarly, P_C and P_{C0} are, respectively, the actual and preferred perimeters of the same cell. In this work, we assumed K_C, Γ_C, A_{C0} , and P_{C0} to be identical for all cells (i.e., $K_C \equiv K, \Gamma_C \equiv \Gamma, A_{C0} \equiv A_0, P_{C0} \equiv P_0$). Furthermore, we fixed the values of K and A_0 , and measured the energy in units of KA_0^2 , stresses in units of KA_0 , and lengths in units of $A_0^{1/2}$. Since the ratio between the perimeter and area elastic moduli does not qualitatively change the behavior of the VM [20, 41], we fixed that ratio to $\Gamma/(KA_0) \approx 0.289$. The only variable parameter in simulations was the preferred cell perimeter P_0 , which sets the dimensionless cell-shape parameter, defined as the ratio $p_0 = P_0/\sqrt{A_0}$.

The cell-shape parameter, p_0 , plays a central role in determining whether the system behaves as a fluid or solid [20]. Bi, *et al.* [20] argued that the rigidity transition occurs at $p_0 = p_c \approx 3.812$ for a random polygonal tiling. The transition point is, however, at $p_c = \sqrt{8\sqrt{3}} \approx 3.722$ for a regular hexagonal tiling [47]. In the fluid phase, the energy barrier for neighbor exchanges vanishes and cells can flow past each other [48]. As p_0 is reduced below p_c , the energy barrier becomes finite, neighbor exchanges cease and the system becomes solid. While the transition point for hexagonal tilings can be understood in terms of the mechanical stability and the excess perimeter [44], the mechanism that leads to a larger value for random tilings is more subtle and not fully understood [49].

For definiteness, in all simulations we always started from a regular hexagonal tiling in a nearly square box subject to periodic boundary conditions, where the initial cell areas A_C matched the preferred areas A_0 (see Methods). For the solid phase with $p_0 \lesssim 3.722$, a hexagonal tiling is the ground state of the energy in Eq. (1) [47] and it was directly used to investigate rheological properties. Note that there was some residual hydrostatic stress (due to the mismatch of cell perimeters P_C from the preferred values P_0), which could be eliminated by the appropriate relaxation of the simulation box. This hydrostatic stress, however, does not qualitatively affect the rheological behavior of the system (see Supplementary Information, Sec. IV for further discussion). For the fluid phase with $p_0 \gtrsim 3.722$, the hexagonal tiling corresponds to a saddle point of the energy in Eq. (1) [47]. Thus a small random perturbation was applied to each vertex by a displacement drawn from the Gaussian distribution with zero mean and standard deviation $1.5 \times 10^{-4}\sqrt{A_0}$ (see Methods) and then the system was relaxed using the FIRE algorithm [50] to reach a local energy minimum. Note that the energy landscape in the fluid phase has many local minima and a large number of soft modes (see Supporting Information, Sec. VIII). Thus we repeated simulations to investigate rheological properties for multiple configurations corresponding to different local energy minima (see Methods).

In order to probe the dynamical response of the VM, we need to specify the microscopic equations of motion for vertices. Assuming the low Reynolds number limit, which is applicable to most cellular systems due to their

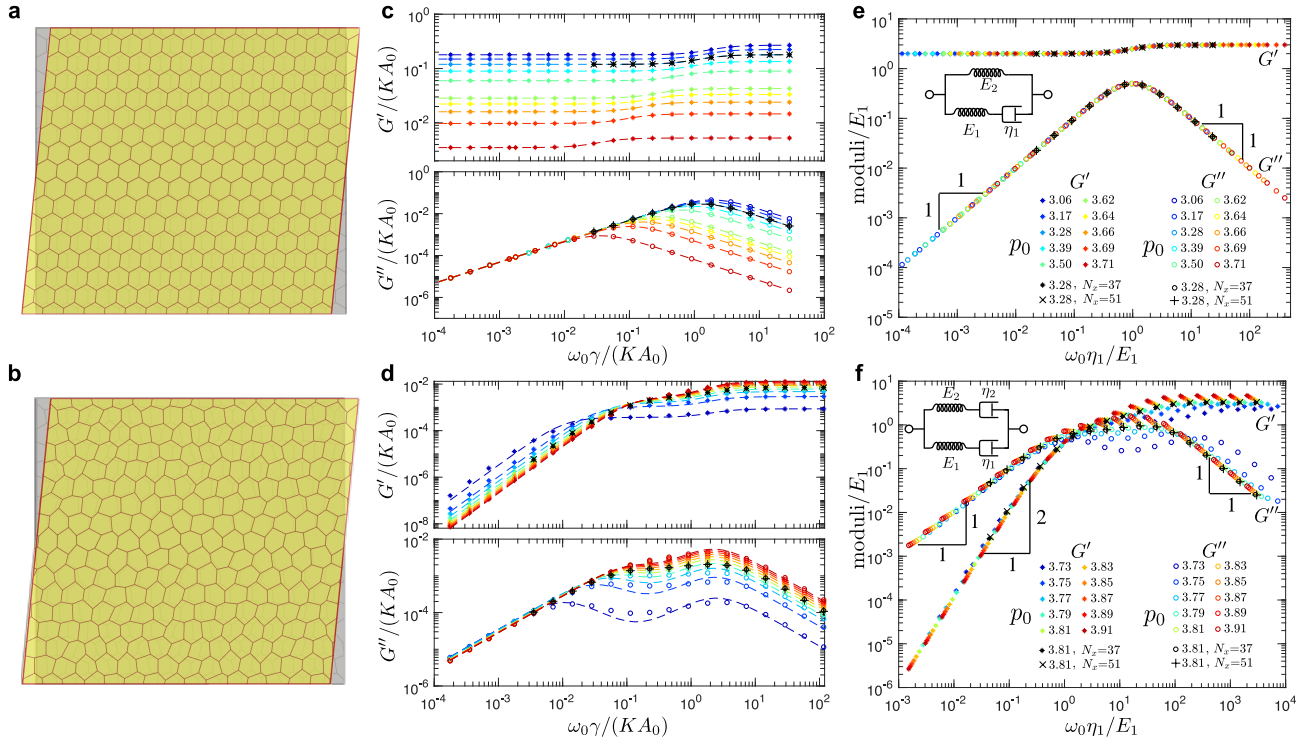


FIG. 1. Loss and storage shear moduli in the solid (top row) and fluid phase (bottom row). An overlay of the representative reference (grey) and sheared (yellow) configurations in (a) the solid and (b) the fluid phase. The magnitude of the shear is highly exaggerated for demonstration purposes. (c-d) show the representative storage (G') and loss (G'') shear moduli as functions of the shearing frequency, ω_0 , for different values of the cell-shape parameter, p_0 , where we removed the dissipative contribution to G'' due to the velocity field resulting from the affine part of the deformation that dominates at large frequencies (see text). Dashed curves are the fits based on (c) the Standard Linear Solid (SLS) model in the solid phase and (d) the Burgers model in the fluid phase. (e-f) The collapse of the moduli curves for different values of p_0 for (e) the solid phase and (f) the fluid phase. The insets show the representation of (e) the SLS model and (f) the Burgers model in terms of the springs and dashpots. The majority of the data corresponds to the system of nearly square shape with $N_x = 15$ cells in the horizontal direction, and we also show examples of larger systems with $N_x = 37$ and $N_x = 51$ cells in the horizontal direction.

slow speed, inertial effects can be neglected [51]. The equations of motion are then a force balance between friction and elastic forces due to deformations of cell shapes, i.e.,

$$\gamma \dot{\mathbf{r}}_i = \mathbf{F}_i. \quad (2)$$

Here, \mathbf{r}_i is the position vector of vertex i in a laboratory frame of reference, $\mathbf{F}_i = -\nabla_{\mathbf{r}_i} E$ is the mechanical force on vertex i due to deformation of cells surrounding it, γ is the friction coefficient, and dot denotes the time derivative. In simulations we fixed the value of γ , which sets the unit of time as $\gamma/(KA_0)$.

We note that a precise model for dissipation in epithelial tissues is at present not known. While having a mechanism of dissipating the external energy input is central in this study, its precise microscopic details are, however, not important. We therefore assume that each vertex experiences dissipative drag proportional to its instantaneous velocity, which is a common assumption in discrete models of soft materials [52]. Furthermore, we neglected thermal fluctuations of vertices and hence omit the stochastic term in Eq. (2). This is a reasonable

assumption since typical energy scales in tissues significantly exceed the thermal energy, $k_B T$, at room temperature T , where k_B is the Boltzmann constant. It is important, however, to note that in epithelia there are other sources of stochasticity (e.g., fluctuations of the number of force-generating molecular motors) that are important for tissue scale behaviors [53]. Here, we do not consider such effects but point out that they could be directly included in the model as additional forces in Eq. (2).

Response to a shear deformation. The hexagonal ground state in the solid phase and states corresponding to local energy minima in the fluid phase were then used to investigate the rheological behavior by applying an oscillatory affine shear deformation (Fig. 1a,b). At each time step, we first applied the affine shear deformation to the simulation box and all vertices that was followed by internal relaxation of vertices according to Eq. (2) (see Methods). The affine shear deformation can be described by a deformation gradient tensor defined as $\hat{\mathbf{F}} = \partial \mathbf{x} / \partial \mathbf{X}_0$, where the mapping $\mathbf{x} = \mathbf{x}(\mathbf{X}_0, t)$ maps the reference configuration \mathbf{X}_0 to a spatial configuration

\mathbf{x} at time t . For simple shear, the deformation gradient tensor is $\hat{\mathbf{F}} = \begin{pmatrix} 1 & \epsilon(t) \\ 0 & 1 \end{pmatrix}$, where $\epsilon(t) = \epsilon_0 \sin(\omega_0 t)$. Sufficiently small amplitude $\epsilon_0 = 10^{-7} \ll 1$ was used to probe the linear response properties.

The response stress tensor, $\hat{\boldsymbol{\sigma}}_C(t)$, for each cell C was computed using the formalism introduced in [54] (see Supplementary Information, Sec. I). The average stress tensor $\hat{\boldsymbol{\sigma}}(t) = \sum_C w_C \hat{\boldsymbol{\sigma}}_C(t)$, with $w_C = A_C / \sum_C A_C$, was used as a measure for the response of the system. The dynamic shear modulus $G^*(\omega_0) = \tilde{\tau}(\omega_0) / \tilde{\epsilon}(\omega_0)$ was then calculated at a given frequency ω_0 of applied shear strain, where $\tilde{\tau}(\omega)$ and $\tilde{\epsilon}(\omega)$ are the Fourier transforms of the response shear stress $\tau(t) = \hat{\sigma}_{xy}(t)$ and the applied strain $\epsilon(t)$, respectively (see Methods). We ensured that the simulations were sufficiently long for a steady state to be reached (see Methods and Supplementary Information, Sec. III). The real part of the dynamic shear modulus, $G' = \text{Re}(G^*)$, is the storage shear modulus and the imaginary part, $G'' = \text{Im}(G^*)$, is the loss shear modulus. The storage shear modulus corresponds to the in-phase response and measures the elastic (i.e., reversible) response of the system, while the loss shear modulus corresponds to the out-of-phase response and measures the irreversible dissipation [55] (see also Supplementary Information, Sec. II). Note that the stress contribution due to the friction with the substrate resulting from the part of the velocity field due to the externally imposed affine deformation was removed in the analysis. This is because at high frequencies, the stresses are dominated by the friction due to external driving that masks the internal material response that we are interested in exploring (see Fig. S3 and Supplementary Information, Sec. I). For systems under an oscillatory simple shear, storage and loss shear moduli were obtained for different values of p_0 and different system sizes in the solid and the fluid phases with frequencies ω_0 of the applied shear strain spanning over seven orders of magnitude, as shown in Fig. 1c,d. Most simulations were performed for systems with nearly square shapes with $N_x = 15$ cells in the horizontal direction. We repeated several simulations for systems with $N_x = 37$ and $N_x = 51$, which showed that the finite size effects are negligible (Fig. 1c-f).

In the solid phase there are two different regimes (see Fig. 1c). At low frequencies, ω_0 , the storage shear modulus G' has a constant value, while the loss shear modulus scales as $G'' \propto \omega_0$. At high frequencies the storage shear modulus G' has a higher constant value, while the loss shear modulus scales as $G'' \propto \omega_0^{-1}$. Such rheological behavior is characteristic for the Standard Linear Solid (SLS) model [55]. Storage and loss shear moduli for the SLS model are [55], respectively,

$$G'_{\text{SLS}}(\omega_0) = \frac{E_2 + \frac{\eta_1^2}{E_1^2} \omega_0^2 (E_1 + E_2)}{1 + \frac{\eta_1^2}{E_1^2} \omega_0^2}, \quad (3a)$$

$$G''_{\text{SLS}}(\omega_0) = \frac{\omega_0 \eta_1}{1 + \frac{\eta_1^2}{E_1^2} \omega_0^2}, \quad (3b)$$

where we used the representation of the SLS model (Fig. 1e, inset) that consists of a spring with elastic constant E_2 connected in parallel with a Maxwell element, which comprises a spring with elastic constant E_1 and a dashpot with viscosity η_1 connected in series. The above expressions in Eqs. (3) were used to fit the storage and loss shear moduli obtained from simulations. The fitted curves, represented with dashed lines in Fig. 1c, show an excellent match with the simulation data, indicating that the SLS model is indeed appropriate to describe the shear rheology in the solid phase. This was also confirmed in Fig. 1e, where we collapsed the storage and loss shear moduli for different values of the shape parameter, p_0 , by rescaling the moduli and frequencies with the fitted values of spring and dashpot constants.

As the value of the p_0 increases, we observe that the storage shear modulus reduces at all frequencies and that the loss shear modulus reduces at high frequencies. Furthermore the crossover between the two regimes shifts towards lower frequencies (Fig. 1c). This is because the elastic constants E_1 and E_2 decrease linearly with increasing p_0 and they become zero exactly at the solid-fluid transition with $p_0 = p_c \approx 3.722$ (Fig. 2a). The dashpot constant η_1 is nearly independent of p_0 and scales with the friction parameter γ , which is the only source of dissipation in the VM. The crossover between the two regimes for both the storage and loss shear moduli corresponds to a characteristic time scale, η_1/E_1 , which diverges as p_0 approaches the solid-fluid transition due to the vanishing elastic constant (Fig. 2c). Note that the values of the elastic constants E_1 and E_2 can be estimated analytically. In the quasistatic limit ($\omega_0 \rightarrow 0$), the external driving is sufficiently slow that the system can relax internally. In this limit, Murisic, *et al.* showed that the storage shear modulus is

$$G'(\omega_0 \rightarrow 0) = E_2 = \frac{1}{2} K A_0 (1 - [\alpha(p_0, \Gamma / K A_0)]^2), \quad (4)$$

where $\alpha(p_0, \Gamma / K A_0)$ is a scaling factor chosen such that the hydrostatic stress vanishes once the system box size is rescaled from L to αL [56]. In the high frequency limit ($\omega_0 \rightarrow \infty$), on the other hand, the system follows the externally imposed affine deformation and has no time for internal relaxation. Thus, by considering the energy cost for a hexagonal tiling under affine deformation, we obtained the storage shear modulus (see Supplemental Information, Sec. VII)

$$G'(\omega_0 \rightarrow \infty) = E_1 + E_2 = 3\sqrt{3}\Gamma \left(1 - \frac{p_0}{p_c}\right). \quad (5)$$

The above Eqs. (4) and (5) were used to extract the values of elastic constants E_1 and E_2 , which showed excellent agreement with the fitted values from simulations (Fig. 2a).

In the fluid phase, the storage and loss shear moduli show a markedly different behavior (Fig. 1d). There are three different regimes with two crossover frequencies,

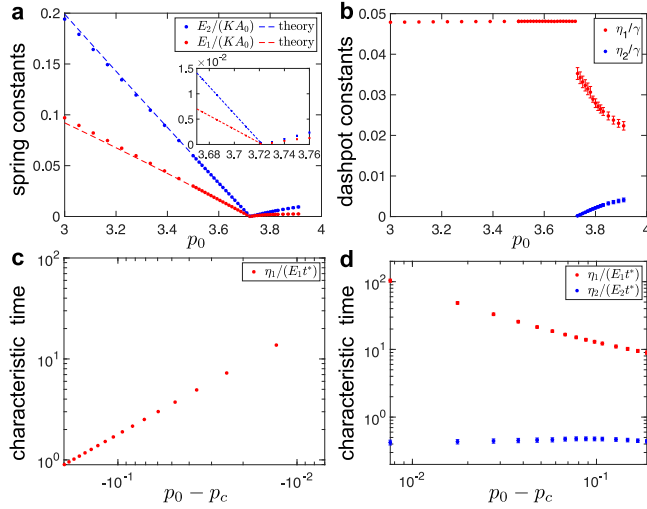


FIG. 2. (a-b) Fitted values of spring-dashpot models for the system under simple shear. (a) Elastic constants as a function of target cell-shape parameter, p_0 . In the solid phase (i.e., for $p_0 < p_c \approx 3.722$), fitted values of the spring constants show excellent match with the analytical predictions obtained from Eqs. (4) and (5) (dashed lines). Inset shows the spring constants near the critical point. (b) Dashpot viscosity constants as a function of the target cell-shape parameter, p_0 . (c-d) Characteristic time scales in (c) the solid and (d) fluid phase obtained from the fitted values of the elastic constant and the dashpot viscosity. The normalization factor $t^* = \gamma/(KA_0)$ sets the unit of time. For the fluid phase (i.e., for $p_0 > p_c \approx 3.722$), errorbars correspond to the standard deviation for simulations that were repeated for configurations that correspond to different local energy minima.

which correspond to two characteristic time scales. At low frequencies, ω_0 , the storage shear modulus $G' \propto \omega_0^2$ and the loss shear modulus $G''(\omega_0) \propto \omega_0$. The storage modulus approaches 0 for $\omega_0 \rightarrow 0$, which indicates that the system is indeed a fluid. At high frequencies the storage shear modulus has a constant value, while the loss shear modulus scales as $G''(\omega_0) \propto \omega_0^{-1}$. To capture this behavior we used the Burgers model, which consists of two Maxwell models connected in parallel (Fig. 1f, inset), to fit the shear moduli measured in the simulations. The storage and loss shear moduli for a Burgers model are [55], respectively,

$$G'_{\text{Burg}}(\omega_0) = \frac{p_1 q_1 \omega_0^2 - q_2 \omega_0^2 (1 - p_2 \omega_0^2)}{p_1^2 \omega_0^2 + (1 - p_2 \omega_0^2)^2}, \quad (6a)$$

$$G''_{\text{Burg}}(\omega_0) = \frac{p_1 q_2 \omega_0^3 + q_1 \omega_0 (1 - p_2 \omega_0^2)}{p_1^2 \omega_0^2 + (1 - p_2 \omega_0^2)^2}, \quad (6b)$$

where $p_1 = \eta_1/E_1 + \eta_2/E_2$, $p_2 = \eta_1 \eta_2/(E_1 E_2)$, $q_1 = \eta_1 + \eta_2$, $q_2 = \eta_1 \eta_2 (E_1 + E_2)/(E_1 E_2)$. The dashed curves in Fig. 1d show fits of the storage and loss shear moduli for a range of values of p_0 , which show good agreement with simulations. Unlike for the solid phase, it is not possible to collapse the data for storage and loss shear moduli onto single universal curves because the fluid phase is

characterized by two independent timescales η_1/E_1 and η_2/E_2 . Thus we show two different collapses for the storage and loss shear moduli in the low frequency range (Fig. 1f) and in the high frequency range (Fig. S7 in the Supplementary Information, Sec. V).

As the value of the p_0 decreases, we observe that both the storage and loss shear moduli reduce at intermediate and high frequencies, but they increase at low frequencies (Fig. 1d). We also observe that the first crossover shifts towards lower frequencies, while the second crossover remains at approximately the same frequency. This is because the elastic constants E_1 and E_2 decrease linearly toward zero as p_0 approaches the solid-fluid transition at $p_c \approx 3.722$ (Fig. 2a). The dashpot constant η_2 also decreases linearly toward zero, while the dashpot constant η_1 increases but remains finite as p_0 approaches the solid-fluid transition (Fig. 2b). As a consequence, one of the characteristic time scales η_1/E_1 diverges, while the second time scale η_2/E_2 remains finite as p_0 approaches the solid-fluid transition (Fig. 2d). The diverging characteristic time scale captures the macroscopic behavior of the system, while the second time scale ($\sim \gamma/KA_0$) captures the microscopic details of the VM. Finally, we note that the values of the spring and dashpot constants are somewhat sensitive to the local energy minimum configuration used to probe the response in the fluid phase. The errorbars in Fig. 2 show standard deviation for different configurations that were obtained by using the same magnitude of the initial perturbation (see Methods). In Fig. S8 in the Supplementary Information, Sec. VI, we show how the values of the spring and dashpot constants are affected when configurations were obtained by using different magnitudes of the initial perturbation.

Response to bulk deformations. We further studied the bulk rheological properties of the system by applying an oscillatory biaxial deformation (Fig. 3a,b) described by the deformation gradient $\hat{\mathbf{F}} = \begin{pmatrix} 1+\epsilon(t) & 0 \\ 0 & 1+\epsilon(t) \end{pmatrix}$, where $\epsilon(t) = \epsilon_0 \sin(\omega_0 t)$. We applied a sufficiently small amplitude $\epsilon_0 = 10^{-7} \ll 1$ to probe the linear response properties characterized by the average normal stress $\sigma(t) = \frac{1}{2} [\hat{\sigma}_{xx}(t) + \hat{\sigma}_{yy}(t)]$, where we again removed the stress contribution due to the friction with the substrate resulting from the part of the velocity field due to the externally imposed affine deformation. As in the simple shear test, we then computed the dynamic bulk modulus as $B^*(\omega_0) = \tilde{\sigma}(\omega_0)/\tilde{\epsilon}(\omega_0)$ from which we obtained the storage bulk modulus $B' = \text{Re}(B^*)$ and the loss bulk modulus $B'' = \text{Im}(B^*)$ (see Fig. 3c,d).

In the solid phase, the storage bulk modulus is independent of the driving frequency and the loss bulk modulus is zero. Thus the response of the system can be captured by a single spring E_{solid} (Fig. 3e, inset). This is because the hexagonal tiling is stable to biaxial deformation in the solid phase and thus there is no internal relaxation. The measured value of the storage bulk modulus matches the analytical prediction

$$B_{\text{theory}} = 2KA_0 + \sqrt{12}\Gamma p_0 \quad (7)$$

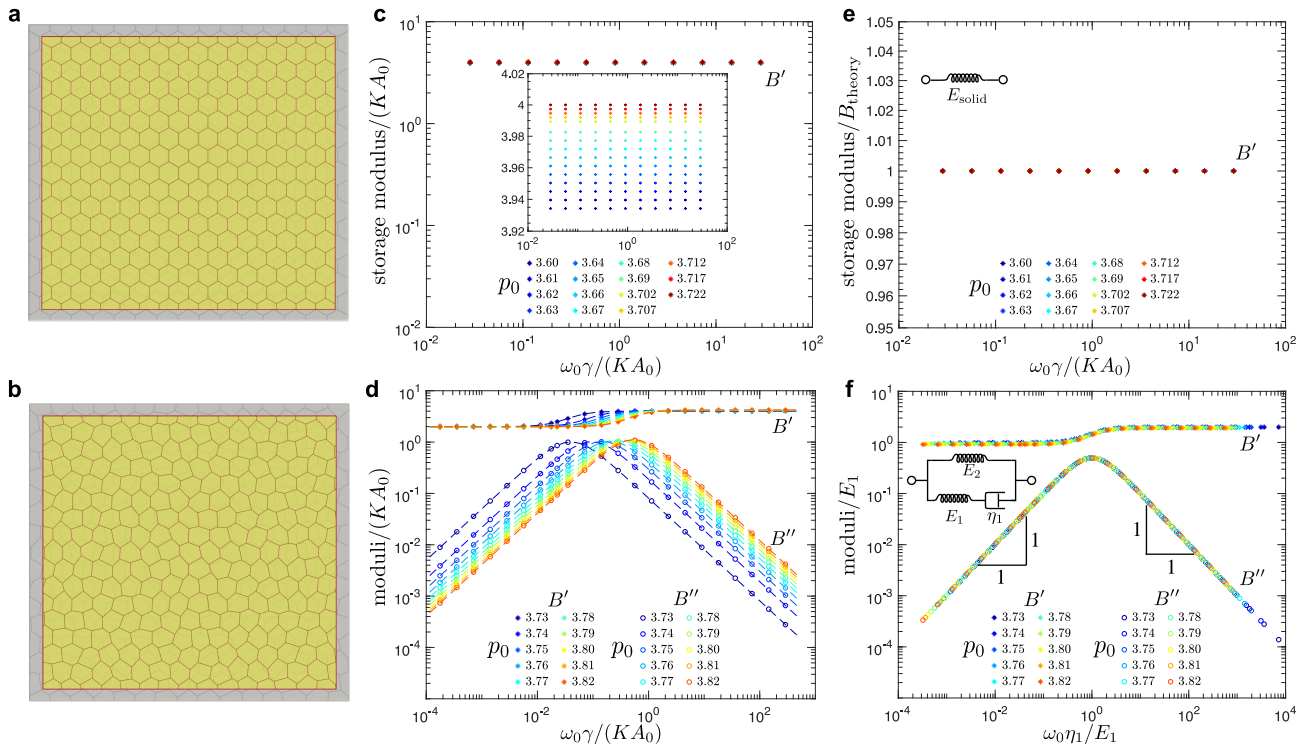


FIG. 3. Loss and storage bulk moduli in the solid (top row) and fluid phase (bottom row). An overlay of the representative reference (grey) and biaxially deformed (yellow) configurations in (a) the solid and (b) the fluid phase. The magnitude of the bulk deformation is highly exaggerated for demonstration purposes. (c-d) show the representative storage (B') and loss (B'') bulk moduli as functions of the deformation frequency, ω_0 , for different values of the cell-shape parameter, p_0 , where we removed the dissipative contribution to B'' due to the velocity field resulting from the affine part of the deformation that dominates at large frequencies (see text). For the solid phase in (c), the loss bulk modulus $B'' \equiv 0$. For the fluid phase in (d), dashed curves are the fits based on the Standard Linear Solid (SLS) model. (e-f) The collapse of the moduli curves for different values of p_0 for (e) the solid phase and (f) the fluid phase. The insets show the representation of (e) the spring model and (f) the SLS model in terms of the springs and dashpots.

by Staple, *et al.* [47], where the hexagonal tiling is assumed to undergo affine deformation under biaxial deformation. Storage bulk moduli, normalized by B_{theory} , for different values of p_0 all collapse to 1 (Fig. 3e).

In the fluid phase, the bulk response behavior of the system can be described by the SLS model (Fig. 3f, inset). While it might appear counter-intuitive to model a fluid with the SLS model, this is a direct consequence of the fact that in the fluid state, the bulk modulus is finite but the shear modulus vanishes, i.e., the fluid flows in response to shear but resists bulk deformation. The fitted storage and loss bulk moduli for the SLS model [see Eq. (3)] show an excellent match with the simulation data (Fig. 3d). This was also confirmed in Fig. 3f, where we collapsed the storage and loss bulk moduli for different values of p_0 .

The fitted values of spring elastic and dashpot viscosity constants for different values of p_0 are plotted in Fig. 4. In the fluid phase, the storage bulk modulus in the high frequency limit ($B'(\omega_0 \rightarrow \infty) = E_1 + E_2$) continuously increases from the value for the solid phase B_{theory} in Eq. (7) as the system transitions from solid to fluid (Fig. 4a). The storage bulk modulus in the quasistatic

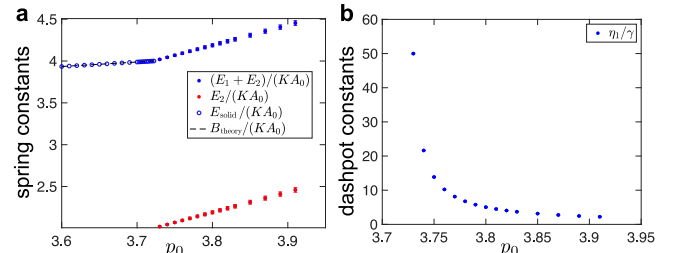


FIG. 4. Fitted values of spring-dashpot models for the system under bulk deformation as a function of the target cell-shape parameter, p_0 . (a) In the solid phase ($p_0 < p_c \approx 3.722$), the bulk storage modulus E_{solid} agrees with the analytical prediction B_{theory} in Eq. (7). At the solid-fluid transition point ($p_0 = p_c \approx 3.722$), it continuously changes to the high frequency limit of the bulk storage modulus, i.e., $B'(\omega_0 \rightarrow \infty) = E_1 + E_2$, of the fluid phase. The low frequency limit of the bulk storage modulus is $B'(\omega_0 \rightarrow 0) = E_1$ in the fluid phase. (b) Dashpot viscosity constant as a function of p_0 . For the fluid phase ($p_0 > p_c \approx 3.722$), errorbars correspond to the standard deviation for simulations that were repeated for configurations that correspond to different local energy minima.

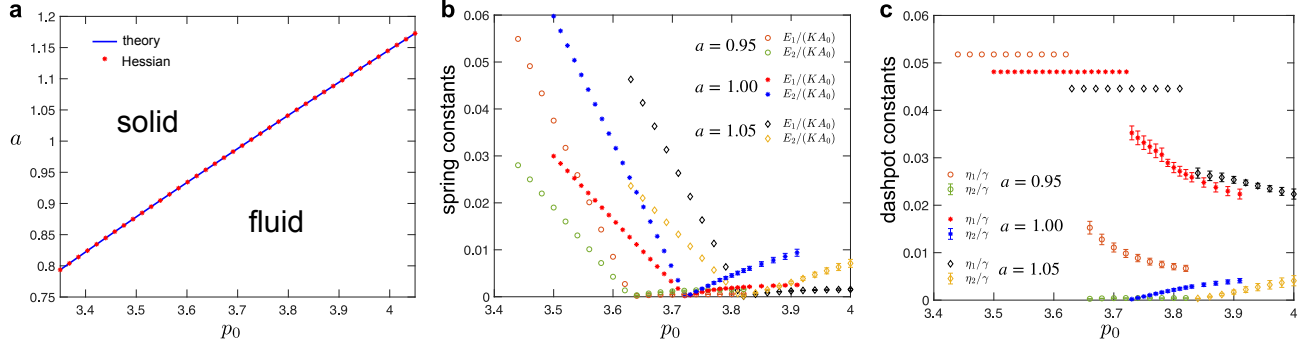


FIG. 5. Tuning the solid to fluid transition by applying uniaxial deformation. (a) The solid-fluid transition boundary in the $a - p_0$ plane, where a measures the amount of uniaxial deformation described by the deformation gradient $\hat{\mathbf{F}} = \begin{pmatrix} a & 0 \\ 0 & 1 \end{pmatrix}$. Blue line shows the analytical prediction from Eq. (9), which matches the stability analysis with the Hessian matrix (red dots). (b,c) The fitted values of the (b) spring and (c) dashpot constants for the SLS model in the solid phase and the Burgers model in the fluid phase when the system is under uniaxial compression ($a = 0.95$), no pre-deformation ($a = 1$), and under uniaxial tension ($a = 1.05$).

limit ($B'(\omega_0 \rightarrow 0) = E_2$) emerges at the transition point with a finite value and increases as p_0 increases from p_c (Fig. 4a). Fig. 4b shows that the dashpot constant diverges as the p_0 decreases toward p_c . Thus, the characteristic time scale η_1/E_1 also diverges, but for a different reason than for the shear deformation, where the spring constant is vanishing (see Fig. 2). Finally, we note that, unlike for the response to shear, the values of the spring and dashpot constants for bulk deformation are not sensitive to the local energy minimum configuration used to probe the response in the fluid phase, which is reflected in very small errorbars in Fig. 4. This is because the bulk moduli are dominated by the changes in cell areas.

Response to a shear deformation of a uniaxially pre-deformed system. The solid-fluid transition for the regular hexagonal tiling occurs when $p_0 \approx 3.722$, above which the hexagonal tiling is unstable. This is consistent with the vanishing of the affine shear modulus in Eq. (5) at the transition point. If the regular hexagonal tiling is compressed or stretched uniaxially by a factor a , which is described by the deformation gradient $\hat{\mathbf{F}} = \begin{pmatrix} a & 0 \\ 0 & 1 \end{pmatrix}$, then the high frequency limit of the storage shear modulus that is dominated by affine deformation becomes (see Supplemental Information, Sec. VII),

$$G'_{\text{affine}}(a) = \frac{2\sqrt{2}\Gamma}{3^{7/4}a} \left(1 + \frac{1}{(1+3a^2)^{3/2}} \right) \times \left(-3p_0 + \sqrt[4]{192} \left(1 + \sqrt{1+3a^2} \right) \right). \quad (8)$$

By setting the affine shear modulus to 0, we obtained the solid-fluid transition boundary in the $a - p_0$ plane as

$$a(p_0) = \sqrt{\frac{\sqrt{3}p_0^2}{8} - \frac{p_0}{\sqrt[4]{12}}}. \quad (9)$$

The above analytical prediction for the phase boundary (Fig. 5a, blue line) shows an excellent agreement with the stability analysis in terms of the eigenvalues of the

Hessian matrix of the energy function (Fig. 5a, red dots). A given configuration is stable if all eigenvalues of the Hessian matrix are positive and the loss of mechanical stability occurs when the lowest eigenvalue becomes 0. For a given p_0 , the value of the lowest eigenvalue reduces with decreasing a , i.e., as the magnitude of compression is increased. Thus, the compression (stretching) shifts the solid-fluid transition towards the lower (higher) values of p_0 (see Fig. 5a).

We also probed the response to oscillatory shear applied to uniaxially compressed and stretched systems. This analysis was done on both the uniaxially deformed hexagonal tiling in the solid phase as well as a system in the fluid phase obtained by relaxing the unstable uniaxially deformed hexagonal tiling after an initial random perturbation (see Methods). The response to the shear deformation is qualitatively similar and can still be described by the SLS model in the solid phase and the Burgers model in the fluid phase. Fig. 5b,c shows fitted values of the parameters for spring-dashpot models when the system is under uniaxial compression ($a = 0.95$), no pre-deformation ($a = 1$, i.e., same as Fig. 2a,b), and uniaxial tension ($a = 1.05$). In both the solid and fluid phases, all spring elastic constants decrease to 0 as p_0 approaches the critical value predicted by Eq. (9). The dashpot viscosity remains constant in the solid phase. Once the system enters the fluid phase as p_0 increases, a new second dashpot constant emerges and increases from 0, while the value of the first dashpot constant decreases. As in the simple shear case, we note that the values of the spring and dashpot constants are somewhat sensitive to the local energy minimum configuration used to probe the response in the fluid phase. The errorbars in Fig. 2 show standard deviation for configurations that were obtained by using different random initial perturbation (see Methods). Finally, we note that besides uniaxial deformation, the solid-fluid transition point can be tuned by other modes of deformation (see Fig. S9 and Supplemen-

Supplementary Information, Sec. VII).

DISCUSSION

We have performed a detailed analysis of the rheological properties of the Vertex Model subject to small-amplitude oscillatory deformations over seven orders of magnitude in the driving frequency. Our analysis shows that the VM exhibits non-trivial viscoelastic behavior that can be tuned by a single dimensionless geometric parameter - the shape parameter, p_0 . In order to characterize the response, we constructed constitutive rheological models that use combinations of linear springs and dashpots connected in series and in parallel. These models allowed us to match the shear response of the VM to that of the Standard Linear Solid model in the solid phase and the Burgers model in the fluid phase. In the low-frequency, i.e., quasistatic regime, our results are fully consistent with many previous studies [20, 21, 47, 56]. Our work, however, provides insights into the time-dependent response of the VM over a broad range of driving frequencies, which is important if one is to develop full understanding of the rheological properties of the VM and how those inform our understanding of the rheology of epithelial tissues.

We also showed that the critical value for the solid-fluid transition can be tuned by applying pre-deformation. Interestingly, under uniaxial and biaxial (i.e., isotropic) compression the solid to fluid transition shifts to lower values of p_0 , leading to the non-intuitive prediction that one can fluidize the system by compressing it. This is, however, not surprising since the transition is driven by a geometric parameter that is inversely proportional to the square root of the cell's native area. Compressing the system reduces its area and, hence, effectively increases p_0 . It is, however, important to note that this is just a property of the VM and it does not necessarily imply that actual epithelial tissue would behave in the same way. Cells are able to adjust their mechanical properties in response to applied stresses and it would be too simplistic to assume that compression would directly lead to changes in the native area. In fact, experiments on human bronchial epithelial cells show that applying apical-to-basal compression, which effectively expands the tissue laterally (i.e., corresponds to stretching in our model) fluidizes the tissue [19].

Furthermore, the transition from solid phase to fluid phase is accompanied by the emergence of a large number of soft modes. As we have already alluded, it has recently been argued that these soft modes lead to a nonlinear response distinct from that obtained in classical models of elasticity [44]. Approximately half of the eigenmodes are zero modes (see Fig. S10 in the Supplementary Information, Sec. VIII). While the analysis of soft modes in the VM is an interesting problem [49], it is beyond the scope of this work. Other models in this class have intriguing non-trivial mechanical properties, such as the existence

of topologically protected modes [57–62].

We note that while we studied the dynamical response over a wide range of frequencies, our work focused on the behavior in the linear response regime, where there are effectively no plastic events, i.e., while being allowed, T1 transformations typically did not occur during the process of probing the rheology. A full understanding of the VM rheology would also need to allow for cell rearrangements. This is, however, a very challenging problem and first steps in addressing it have only recently been made [45].

Regardless of whether cells in an epithelial tissue are arrested or able to move, the rheological response of the tissue is viscoelastic with multiple time scales [38]. This response arises as a result of the complex material properties of individual cells combined with four basic cellular behaviors: movement, shape change, division, and differentiation. The tissue not only has a non-trivial rheological response but is also able to tune it. There is growing evidence that this ability of biological systems to tune their rheology, and in particular, transition between solid-like and fluid-like behaviors, plays a key role during morphogenesis [4]. How such cellular processes are regulated and coordinated to form complex morphological structures is only partly understood. It is, however, clear that the process involves mechano-chemical feedback between mechanical stresses and the expression of genes that control the force-generating molecular machinery in the cell. Any models that aim to describe morphological processes, therefore, need to include coupling between biochemical processes and mechanical response. The base mechanical model, however, must be able to capture the underlying viscoelastic nature of tissues. Our work provides evidence that the vertex model, a commonly used model to study mechanics of epithelial tissues, has interesting non-trivial rheological behavior. This, combined with its ability to capture both fluid- and solid-like behavior by tuning a single geometric parameter shows it to be an excellent base model to build more complex descriptions of real tissues.

METHODS

Most simulations were performed for systems with nearly square shapes with $N_x = 15$ cells in horizontal direction (i.e., $N = 240$ cells in total) subject to periodic boundary conditions. The shape of the simulation box was chosen to be as near to a square as allowed by the geometry of a hexagon and the size of the box was such that it accommodated N cells of area A_C that matched the preferred areas A_0 . Simulations of larger system sizes ($N_x = 37, 51$, i.e., $N = 1406, 2652$ cells, respectively) were performed for a subset of values of p_0 to explore the finite size effects. No quantitative differences between the system with $N = 240$ cells and larger systems were observed. Since the ratio between the perimeter and elastic moduli does not qualitatively change the behavior of the

VM [20, 41], we used $\Gamma/(KA_0) \approx 0.289$ for all simulations.

We applied an oscillatory affine deformation of frequency ω_0 either as simple shear described by the deformation gradient $\hat{\mathbf{F}} = \begin{pmatrix} 1 & \epsilon(t) \\ 0 & 1 \end{pmatrix}$ or biaxial deformation described by $\hat{\mathbf{F}} = \begin{pmatrix} 1+\epsilon(t) & 0 \\ 0 & 1+\epsilon(t) \end{pmatrix}$, where $\epsilon(t) = \epsilon_0 \sin(\omega_0 t)$. In all simulations, we used a small magnitude of deformation, i.e., $\epsilon_0 = 10^{-7}$, so that we probed the linear response and the measured moduli were independent of the magnitude of the deformation. In every time step, the system evolved according to the overdamped dynamics in Eq. (2) after the affine deformation was applied. Equations of motion were integrated using the first order Euler method with the time step, $\Delta t \approx 0.00866\gamma/(KA_0)$. Measurements of the response stresses for each cell and the entire system were taken 25 times within each cycle of oscillatory deformation by using Eq. (S17) in the Supporting Information, Sec. I.

To ensure that we were probing the steady state, we performed the following analysis. For example, in the case of shear deformation, the shear stress signal $\tau(t)$ was divided into blocks of length $T = 3T_0$, each containing 3 cycles of the time period $T_0 = 2\pi/\omega_0$ of the driving shear deformation. Within each block n , we performed the Fourier transform of $\tau(t)$ and obtained $\tilde{\tau}_n(\omega)$ as

$$\tilde{\tau}_n(\omega) = \frac{1}{T} \int_{(n-1)T}^{nT} \tau(t) e^{i\omega t} dt, \quad (10)$$

where n is a positive integer. Similar Fourier transform analysis was performed for the strain, $\epsilon(t)$. The length of the simulation was chosen such that it contained a sufficient number of blocks in order for the $\tilde{\tau}_n(\omega_0)$ to reach a steady state value $\tilde{\tau}(\omega_0)$. The obtained steady state value of $\tilde{\tau}(\omega_0)$ was used to calculate the storage and loss shear moduli as described in the main text. Analogous procedure was applied to the normal stress, $\sigma(t)$, in the case of the bulk deformation. Please refer to the Supplementary Information, Sec. III for a representative example of the steady state analysis.

In the solid phase, we performed rheological tests on a hexagonal tiling. In the fluid phase, however, the hexagonal tiling is unstable. Instead, the hexagonal tiling was randomly perturbed and then relaxed to a nearby local stable state using the FIRE optimizer [50]. The local energy minimum was determined with the relative accuracy of 10^{-12} . A random perturbation was applied to each vertex i , i.e., each vertex was displaced from its original position in the hexagonal tiling by a vector $\delta\mathbf{r}_i = \delta x_i \mathbf{e}_x + \delta y_i \mathbf{e}_y$, where x_i and y_i were Gaussian ran-

dom variables with zero mean and standard deviation $1.5 \times 10^{-4}\sqrt{A_0}$. The rheology of a local stable state was then probed following the same procedure as in the solid case.

During the energy minimization and oscillatory deformations, T1 transitions were allowed but were not common. T1 transitions were implemented following the procedure introduced by Spencer, *et al.* [63].

ACKNOWLEDGEMENTS

This research was primarily supported by NSF through the Princeton University’s Materials Research Science and Engineering Center DMR-2011750 and by the Project X Innovation Research Grant from the Princeton School of Engineering and Applied Science. RS acknowledges support by the UK BBSRC (Award BB/N009789/1). This project was initiated during the KITP program “Symmetry, Thermodynamics and Topology in Active Matter” (ACTIVE20), and it is supported in part by the National Science Foundation under Grant No. NSF PHY-1748958. We would like to acknowledge useful discussions with Mikko Haataja.

DATA AVAILABILITY

The data supporting the results and findings of this study is available from the corresponding authors upon reasonable request.

CODE AVAILABILITY

Simulation and analysis codes used in this study are available from the corresponding authors upon reasonable request.

CONTRIBUTIONS

ST, RS, and AK conceived the study and designed the project. ST and NS performed numerical simulations and analysed the data. RS developed the Vertex Model code used in numerical simulations. ST, NS, RS, and AK wrote the paper.

COMPETING INTERESTS

The authors declare no competing interests.

[1] T. Lecuit, P.-F. Lenne, and E. Munro, Force generation, transmission, and integration during cell and tissue morphogenesis, *Annual Review of Cell and Developmental Biology* **27**, 157 (2011).

[2] C.-P. Heisenberg and Y. Bellaïche, Forces in tissue morphogenesis and patterning, *Cell* **153**, 948 (2013).

[3] E. Hannezo and C.-P. Heisenberg, Mechanochemical feedback loops in development and disease, *Cell* **178**, 12

(2019).

[4] N. I. Petridou and C.-P. Heisenberg, Tissue rheology in embryonic organization, *The EMBO Journal* **38**, e102497 (2019).

[5] M. H. Ross and W. Pawlina, *Histology* (Lippincott Williams & Wilkins, 2006).

[6] D. Krndija, F. El Marjou, B. Guirao, S. Richon, O. Leroy, Y. Bellaïche, E. Hannezo, and D. M. Vignjevic, Active cell migration is critical for steady-state epithelial turnover in the gut, *Science* **365**, 705 (2019).

[7] L. Wolpert, C. Tickle, and A. M. Arias, *Principles of development* (Oxford University Press, USA, 2015).

[8] R. A. Weinberg, *The biology of cancer* (Garland Science, 2013).

[9] G. Forgacs, R. A. Foty, Y. Shafrir, and M. S. Steinberg, Viscoelastic properties of living embryonic tissues: a quantitative study, *Biophysical Journal* **74**, 2227 (1998).

[10] M. Marchetti, J. Joanny, S. Ramaswamy, T. Liverpool, J. Prost, M. Rao, and R. A. Simha, Hydrodynamics of soft active matter, *Reviews of Modern Physics* **85**, 1143 (2013).

[11] P. Friedl and D. Gilmour, Collective cell migration in morphogenesis, regeneration and cancer, *Nature Reviews Molecular Cell Biology* **10**, 445 (2009).

[12] R. Alert and X. Trepaut, Physical models of collective cell migration, *Annual Review of Condensed Matter Physics* **11**, 77 (2020).

[13] M. Poujade, E. Grasland-Mongrain, A. Hertzog, J. Jouanneau, P. Chavrier, B. Ladoux, A. Buguin, and P. Silberzan, Collective migration of an epithelial monolayer in response to a model wound, *Proceedings of the National Academy of Sciences* **104**, 15988 (2007).

[14] X. Trepaut, M. R. Wasserman, T. E. Angelini, E. Millet, D. A. Weitz, J. P. Butler, and J. J. Fredberg, Physical forces during collective cell migration, *Nature Physics* **5**, 426 (2009).

[15] D. T. Tambe, C. C. Hardin, T. E. Angelini, K. Rajendran, C. Y. Park, X. Serra-Picamal, E. H. Zhou, M. H. Zaman, J. P. Butler, D. A. Weitz, *et al.*, Collective cell guidance by cooperative intercellular forces, *Nature Materials* **10**, 469 (2011).

[16] A. Brugués, E. Anon, V. Conte, J. H. Veldhuis, M. Gupta, J. Colombelli, J. J. Muñoz, G. W. Brodland, B. Ladoux, and X. Trepaut, Forces driving epithelial wound healing, *Nature Physics* **10**, 683 (2014).

[17] R. Etournay, M. Popović, M. Merkel, A. Nandi, C. Blasse, B. Aigouy, H. Brandl, G. Myers, G. Salbreux, F. Jülicher, *et al.*, Interplay of cell dynamics and epithelial tension during morphogenesis of the drosophila pupal wing, *eLife* **4**, e07090 (2015).

[18] T. E. Angelini, E. Hannezo, X. Trepaut, M. Marquez, J. J. Fredberg, and D. A. Weitz, Glass-like dynamics of collective cell migration, *Proceedings of the National Academy of Sciences* **108**, 4714 (2011).

[19] J.-A. Park, J. H. Kim, D. Bi, J. A. Mitchel, N. T. Qazvini, K. Tantisira, C. Y. Park, M. McGill, S.-H. Kim, B. Gweon, *et al.*, Unjamming and cell shape in the asthmatic airway epithelium, *Nature Materials* **14**, 1040 (2015).

[20] D. Bi, J. Lopez, J. M. Schwarz, and M. L. Manning, A density-independent rigidity transition in biological tissues, *Nature Physics* **11**, 1074 (2015).

[21] D. Bi, X. Yang, M. C. Marchetti, and M. L. Manning, Motility-driven glass and jamming transitions in biological tissues, *Physical Review X* **6**, 021011 (2016).

[22] L. Atia, D. Bi, Y. Sharma, J. A. Mitchel, B. Gweon, S. A. Koehler, S. J. DeCamp, B. Lan, J. H. Kim, R. Hirsch, *et al.*, Geometric constraints during epithelial jamming, *Nature Physics* **14**, 613 (2018).

[23] D. M. Sussman, M. Paoluzzi, M. C. Marchetti, and M. L. Manning, Anomalous glassy dynamics in simple models of dense biological tissue, *EPL (Europhysics Letters)* **121**, 36001 (2018).

[24] M. Czajkowski, D. M. Sussman, M. C. Marchetti, and M. L. Manning, Glassy dynamics in models of confluent tissue with mitosis and apoptosis, *Soft Matter* **15**, 9133 (2019).

[25] S. Henkes, K. Kostanjevec, J. M. Collinson, R. Sknepnek, and E. Bertin, Dense active matter model of motion patterns in confluent cell monolayers, *Nature Communications* **11**, 1 (2020).

[26] B. Szabo, G. Szöllösi, B. Gönci, Z. Jurányi, D. Selmeczi, and T. Vicsek, Phase transition in the collective migration of tissue cells: experiment and model, *Physical Review E* **74**, 061908 (2006).

[27] M. Sadati, N. T. Qazvini, R. Krishnan, C. Y. Park, and J. J. Fredberg, Collective migration and cell jamming, *Differentiation* **86**, 121 (2013).

[28] S. Garcia, E. Hannezo, J. Elgeti, J.-F. Joanny, P. Silberzan, and N. S. Gov, Physics of active jamming during collective cellular motion in a monolayer, *Proceedings of the National Academy of Sciences* **112**, 15314 (2015).

[29] M. Merkel and M. L. Manning, A geometrically controlled rigidity transition in a model for confluent 3d tissues, *New Journal of Physics* **20**, 022002 (2018).

[30] J. A. Mitchel, A. Das, M. J. O'Sullivan, I. T. Stancil, S. J. DeCamp, S. Koehler, O. H. Ocaña, J. P. Butler, J. J. Fredberg, M. A. Nieto, *et al.*, In primary airway epithelial cells, the unjamming transition is distinct from the epithelial-to-mesenchymal transition, *Nature Communications* **11**, 1 (2020).

[31] B. Bénazéraf, P. Francois, R. E. Baker, N. Denans, C. D. Little, and O. Pourquié, A random cell motility gradient downstream of fgf controls elongation of an amniote embryo, *Nature* **466**, 248 (2010).

[32] A. K. Lawton, A. Nandi, M. J. Stulberg, N. Dray, M. W. Sneddon, W. Pontius, T. Emonet, and S. A. Holley, Regulated tissue fluidity steers zebrafish body elongation, *Development* **140**, 573 (2013).

[33] A. Mongera, P. Rowghanian, H. J. Gustafson, E. Shelton, D. A. Kealhofer, E. K. Carn, F. Serwane, A. A. Lucio, J. Giammona, and O. Campàs, A fluid-to-solid jamming transition underlies vertebrate body axis elongation, *Nature* **561**, 401 (2018).

[34] N. Desprat, A. Guiroy, and A. Asnacios, Microplates-based rheometer for a single living cell, *Review of Scientific Instruments* **77**, 055111 (2006).

[35] G. Salbreux, G. Charras, and E. Paluch, Actin cortex mechanics and cellular morphogenesis, *Trends in Cell Biology* **22**, 536 (2012).

[36] H. Berthoumieux, J.-L. Maître, C.-P. Heisenberg, E. K. Paluch, F. Jülicher, and G. Salbreux, Active elastic thin shell theory for cellular deformations, *New Journal of Physics* **16**, 065005 (2014).

[37] A. R. Harris, L. Peter, J. Bellis, B. Baum, A. J. Kabla, and G. T. Charras, Characterizing the mechanics of cultured cell monolayers, *Proceedings of the National Academy of Sciences* **109**, 16449 (2012).

[38] A. Bonfanti, J. Fouchard, N. Khalilgharibi, G. Charras, and A. Kabla, A unified rheological model for cells and cellularised materials, *Royal Society Open Science* **7**, 190920 (2020).

[39] D. Matoz-Fernandez, E. Agoritsas, J.-L. Barrat, E. Bertin, and K. Martens, Nonlinear rheology in a model biological tissue, *Physical Review Letters* **118**, 158105 (2017).

[40] T. Nagai and H. Honda, A dynamic cell model for the formation of epithelial tissues, *Philosophical Magazine B* **81**, 699 (2001).

[41] R. Farhadifar, J.-C. Röper, B. Aigouy, S. Eaton, and F. Jülicher, The influence of cell mechanics, cell-cell interactions, and proliferation on epithelial packing, *Current Biology* **17**, 2095 (2007).

[42] A. G. Fletcher, M. Osterfield, R. E. Baker, and S. Y. Shvartsman, Vertex models of epithelial morphogenesis, *Biophysical Journal* **106**, 2291 (2014).

[43] D. L. Barton, S. Henkes, C. J. Weijer, and R. Sknepnek, Active vertex model for cell-resolution description of epithelial tissue mechanics, *PLoS Computational Biology* **13**, e1005569 (2017).

[44] M. Moshe, M. J. Bowick, and M. C. Marchetti, Geometric frustration and solid-solid transitions in model 2d tissue, *Physical Review Letters* **120**, 268105 (2018).

[45] M. Popović, V. Druelle, N. Dye, F. Jülicher, and M. Wyart, Inferring the flow properties of epithelial tissues from their geometry, *New Journal of Physics* **xx**, accepted manuscript (2020).

[46] I. Tah, T. Sharp, A. Liu, and D. M. Sussman, Quantifying the link between local structure and cellular rearrangements using information in models of biological tissues, *Soft Matter* (2021).

[47] D. Staple, R. Farhadifar, J.-C. Röper, B. Aigouy, S. Eaton, and F. Jülicher, Mechanics and remodelling of cell packings in epithelia, *The European Physical Journal E* **33**, 117 (2010).

[48] D. Bi, J. H. Lopez, J. Schwarz, and M. L. Manning, Energy barriers and cell migration in densely packed tissues, *Soft Matter* **10**, 1885 (2014).

[49] L. Yan and D. Bi, Multicellular rosettes drive fluid-solid transition in epithelial tissues, *Physical Review X* **9**, 011029 (2019).

[50] E. Bitzek, P. Koskinen, F. Gähler, M. Moseler, and P. Gumbsch, Structural relaxation made simple, *Physical Review Letters* **97**, 170201 (2006).

[51] E. M. Purcell, Life at low reynolds number, *American journal of physics* **45**, 3 (1977).

[52] D. Frenkel and B. Smit, *Understanding molecular simulation: from algorithms to applications*, Vol. 1 (Elsevier, 2001).

[53] S. Curran, C. Strandkvist, J. Bathmann, M. de Gennes, A. Kabla, G. Salbreux, and B. Baum, Myosin ii controls junction fluctuations to guide epithelial tissue ordering, *Developmental Cell* **43**, 480 (2017).

[54] A. Nestor-Bergmann, G. Goddard, S. Woolner, and O. E. Jensen, Relating cell shape and mechanical stress in a spatially disordered epithelium using a vertex-based model, *Mathematical Medicine and Biology: A Journal of the IMA* **35**, i1 (2018).

[55] R. G. Larson, *The structure and rheology of complex fluids*, Vol. 150 (Oxford University Press New York, 1999).

[56] N. Murisic, V. Hakim, I. G. Kevrekidis, S. Y. Shvartsman, and B. Audoly, From discrete to continuum mod- els of three-dimensional deformations in epithelial sheets, *Biophysical Journal* **109**, 154 (2015).

[57] C. Kane and T. Lubensky, Topological boundary modes in isostatic lattices, *Nature Physics* **10**, 39 (2014).

[58] T. Lubensky, C. Kane, X. Mao, A. Souslov, and K. Sun, Phonons and elasticity in critically coordinated lattices, *Reports on Progress in Physics* **78**, 073901 (2015).

[59] J. Paulose, B. G.-g. Chen, and V. Vitelli, Topological modes bound to dislocations in mechanical metamaterials, *Nature Physics* **11**, 153 (2015).

[60] S. D. Huber, Topological mechanics, *Nature Physics* **12**, 621 (2016).

[61] D. Z. Rocklin, S. Zhou, K. Sun, and X. Mao, Transformable topological mechanical metamaterials, *Nature Communications* **8**, 1 (2017).

[62] X. Mao and T. C. Lubensky, Maxwell lattices and topological mechanics, *Annual Review of Condensed Matter Physics* **9**, 413 (2018).

[63] M. A. Spencer, Z. Jabeen, and D. K. Lubensky, Vertex stability and topological transitions in vertex models of foams and epithelia, *The European Physical Journal E* **40**, 2 (2017).

Linear Viscoelastic Properties of the Vertex Model for Epithelial Tissues

Supplementary Information

I. STRESS TENSOR FOR EACH CELL IN THE VERTEX MODEL

The expression for the stress tensor of the vertex model (VM) follows for the most part the derivation in the Ref. [54] in the main text, but there is one important difference as discussed below. For completeness, we here reproduce the key steps of the calculation. The energy functional of the VM can be rewritten as

$$E = \sum_C \left[\frac{K}{2} (A_C - A_0)^2 + \frac{\Gamma}{2} P_C^2 - \Lambda P_C \right], \quad (\text{S1})$$

where we have defined $\Lambda = \Gamma P_0$ and we have omitted the constant term $\frac{1}{2}\Gamma(P_0)^2$ compared to the Eq. (1) in the main text. Other variables have the same meaning as in the main text. Force on the vertex i is then given as

$$\mathbf{F}_i = -\nabla_{\mathbf{r}_i} E = \mathbf{F}_i^{\text{area}} + \mathbf{F}_i^{\text{perim}}, \quad (\text{S2})$$

where $\mathbf{F}_i^{\text{area}}$ and $\mathbf{F}_i^{\text{perim}}$ are the contributions to the force due to area and perimeter terms, respectively. If we introduce pressure

$$p_C = -K (A_C - A_0), \quad (\text{S3})$$

for a cell C then it is straightforward to show that

$$\mathbf{F}_i^{\text{area}} = \sum_e \frac{1}{2} (p_{C_{e,r}} - p_{C_{e,l}}) \mathbf{e}_z \times \mathbf{l}_e \equiv \sum_C \mathbf{f}_{i,C}^{\text{area}}, \quad (\text{S4})$$

and

$$\mathbf{F}_i^{\text{perim}} = \sum_e (\Gamma (P_{C_{e,l}} + P_{C_{e,r}}) - 2\Lambda) \hat{\mathbf{l}}_e \equiv \sum_C \mathbf{f}_{i,C}^{\text{perim}}. \quad (\text{S5})$$

In these expressions, the e -sum loops over the edges originating at vertex i in the clockwise direction, index $C_{e,l}$ ($C_{e,r}$) corresponds to the cell being to the left (right) of edge e when looking away from the vertex i , and \mathbf{l}_e is a vector pointing along the edge e , whose magnitude is equal to the length of the edge (Fig. S1a). \mathbf{e}_z is the unit-length vector perpendicular to the plane of the cell sheet that is assumed to be in the xy plane. Finally, hat $\hat{\cdot}$ denotes unit-length vectors. The summations over edges in Eqs. (S4) and (S5) couple neighboring cells that share a junction, and they can be rewritten to equations in terms of contributions of individual cells to a force on a given vertex. Using the

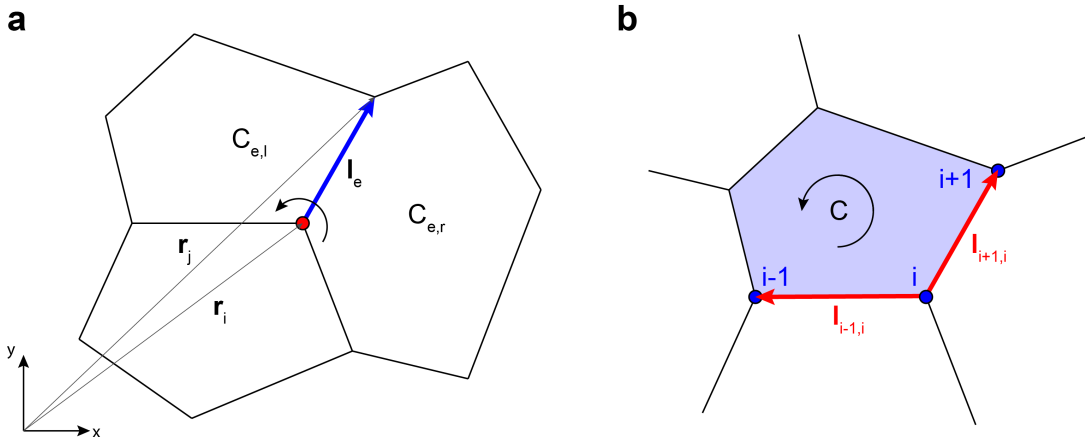


FIG. S1. (a) Blue arrow denotes an edge vector \mathbf{l}_e shared by cells $C_{e,l}$ and $C_{e,r}$. The arc arrow marks the direction in which terms are summed in Eqs. (S4) and (S5). (b) Vertices in a cell are ordered in the counterclockwise direction and red arrows show the definitions for edge vectors between the neighboring vertices.

relation $\nabla_{\mathbf{r}_i} A_C = \frac{1}{2} \mathbf{e}_z \times (\mathbf{l}_{i-1,i} - \mathbf{l}_{i+1,i})$, where $\mathbf{l}_{i\pm 1,i}$ denotes the edge vector between the vertex i and the neighboring vertex $i \pm 1$ of the cell C counted in the counterclockwise directions (Fig. S1b), gives

$$\mathbf{f}_{i,C}^{\text{area}} = \frac{1}{2} \delta_{C,i} p_C \mathbf{e}_z \times (\mathbf{l}_{i-1,i} - \mathbf{l}_{i+1,i}), \quad (\text{S6})$$

where $\delta_{C,i} = 1$ if the vertex i belongs to cell C and $\delta_{C,i} = 0$ otherwise. Similarly, we find the perimeter component of the force of cell C on the vertex i as

$$\mathbf{f}_{i,C}^{\text{perim}} = \delta_{C,i} (\Gamma P_C - \Lambda) (\hat{\mathbf{l}}_{i-1,i} + \hat{\mathbf{l}}_{i+1,i}). \quad (\text{S7})$$

Further, using the assumption that dissipative force on vertex i is equally distributed on neighboring cells, we have that the dissipative force on vertex i with coordination number z_i due to cell C is $\mathbf{f}_{i,C}^{\text{dissip}} = -\gamma \mathbf{v}_i / z_i$. In the overdamped limit, the total mechanical force on each cell is balanced by dissipative forces, so for vertex i , the total mechanical force $\mathbf{f}_i = \mathbf{F}_i^{\text{area}} + \mathbf{F}_i^{\text{perim}}$ is balanced by the dissipative forces (see Fig. S2), i.e.

$$\mathbf{f}_i - \frac{1}{z_i} \gamma \mathbf{v}_i \sum_C \delta_{C,i} = \mathbf{f}_i - \gamma \mathbf{v}_i = 0, \quad (\text{S8})$$

where \mathbf{v}_i is the velocity of vertex i . However, this is not the case for components of vertex forces due to individual cells. In order to construct the stress tensor defined for a cell, we need to change perspective and account for all the forces acting on the cell from the surroundings. The resultant force $\mathbf{F}_{C,i}$ on the cell C due to the vertex i is

$$\mathbf{F}_{C,i} = \mathbf{f}_{C,i} - \frac{1}{z_i} \gamma \mathbf{v}_i \delta_{C,i} = -\mathbf{f}_{i,C} - \frac{1}{z_i} \gamma \mathbf{v}_i \delta_{C,i}, \quad (\text{S9})$$

where we used the 3rd Newton's law to relate the elastic part of the force $\mathbf{f}_{C,i}$ from the vertex i acting on cell C to the equal and opposite force $\mathbf{f}_{i,C} = \mathbf{f}_{i,C}^{\text{area}} + \mathbf{f}_{i,C}^{\text{perim}}$ from the cell C acting on the vertex i . This change of sign is the difference compared to the Ref. [54]. Note that the viscous drag force $-\frac{1}{z_i} \gamma \mathbf{v}_i \delta_{C,i}$ acts at the external force on the cell and we thus keep the same sign.

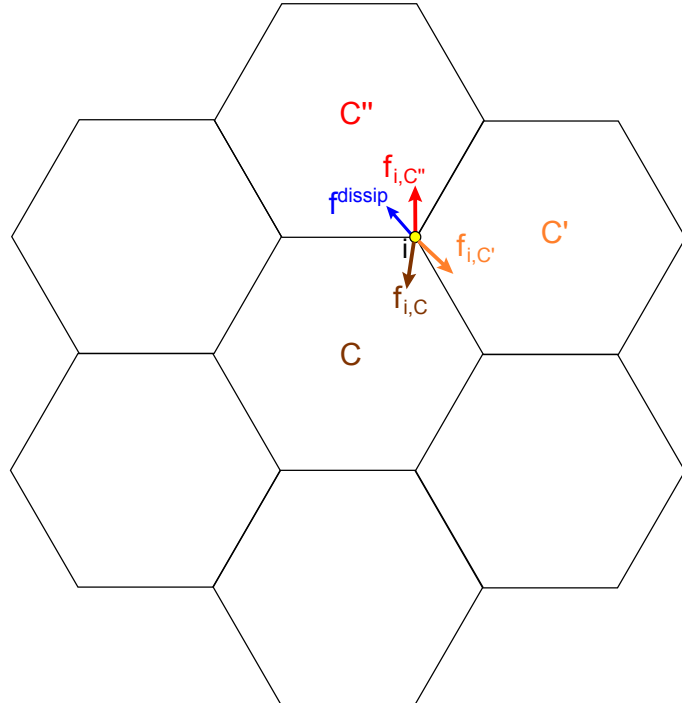


FIG. S2. At vertex i , the total mechanical force, $f_{i,C} + f_{i,C'} + f_{i,C''}$, in terms of the sum of the contributions from individual cells, is balanced by the dissipative force, f_{dissip} , from the external environment.

Before continuing, we introduce the geometric centre of the cell with Z_C vertices as $\mathbf{r}_C = \frac{1}{Z_C} \sum_{i \in C} \mathbf{r}_i$, its velocity as $\mathbf{v}_C = \dot{\mathbf{r}}_C = \frac{1}{Z_C} \sum_{i \in C} \mathbf{v}_i$, and the position of vertex i relative to the cell center C as $\tilde{\mathbf{r}}_i = \mathbf{r}_i - \mathbf{r}_C$. Thus we can compute the total force on the cell C as

$$\mathbf{F}_C = \sum_{i=1}^{Z_C} \mathbf{F}_{C,i} = \sum_{i=1}^{Z_C} \left(-\mathbf{f}_{i,C} - \gamma \frac{1}{z_i} \mathbf{v}_i \right) = \mathbf{f}_C - \gamma \frac{Z_C}{z_i} \mathbf{v}_C = 0, \quad (\text{S10})$$

which is equal to zero due to the overdamped limit.

We can now construct the stress tensor. For a tensor $\hat{\boldsymbol{\sigma}}$ that is symmetric and divergence-free, defined over an area A with perimeter ∂A , we have $\hat{\boldsymbol{\sigma}} = \nabla \cdot (\mathbf{R} \otimes \hat{\boldsymbol{\sigma}})$, where \mathbf{R} is an arbitrary position vector. Thus, we write

$$\int_A \hat{\boldsymbol{\sigma}} dA = \int_A \nabla \cdot (\mathbf{R} \otimes \hat{\boldsymbol{\sigma}}) dA = \int_{\partial A} \mathbf{R} \otimes \hat{\boldsymbol{\sigma}} \cdot \hat{\mathbf{n}} dl, \quad (\text{S11})$$

where we used the Stokes theorem to convert the integral over area A into the integral over the boundary ∂A with the outwards pointing unit normal vector $\hat{\mathbf{n}}$ and the length element dl . If we note that $\hat{\boldsymbol{\sigma}} \cdot \mathbf{n}$ is the force density acting on the boundary and assume that stress is constant over the entire area of the cell, then the Eq. (S11) can be rewritten as

$$\begin{aligned} A_C \hat{\boldsymbol{\sigma}}_C &= \sum_{i \in C} \mathbf{r}_i \otimes \mathbf{F}_{C,i} = \sum_{i \in C} (\mathbf{r}_C + \tilde{\mathbf{r}}_i) \otimes \mathbf{F}_{C,i} = \mathbf{r}_C \otimes \sum_{i \in C} \mathbf{F}_{C,i} + \sum_{i \in C} \tilde{\mathbf{r}}_i \otimes \mathbf{F}_{C,i} \\ A_C \hat{\boldsymbol{\sigma}}_C &= \mathbf{r}_C \otimes \mathbf{F}_C + \sum_{i \in C} \tilde{\mathbf{r}}_i \otimes \left[-\mathbf{f}_{i,C} - \gamma \frac{1}{z_i} \mathbf{v}_i \right] = \sum_{i \in C} \tilde{\mathbf{r}}_i \otimes \left[-\mathbf{f}_{i,C} - \gamma \frac{1}{z_i} \mathbf{v}_i \right]. \end{aligned} \quad (\text{S12})$$

Therefore the stress tensor $\hat{\boldsymbol{\sigma}}_C$ for cell C is

$$\begin{aligned} \hat{\boldsymbol{\sigma}}_C &= \frac{1}{A_C} \sum_{i \in C} \tilde{\mathbf{r}}_i \otimes \left[-\mathbf{f}_{i,C} - \gamma \frac{1}{z_i} \mathbf{v}_i \right], \\ \hat{\boldsymbol{\sigma}}_C &= -\frac{1}{A_C} \sum_{i \in C} \tilde{\mathbf{r}}_i \otimes \left(\frac{1}{2} p_C \mathbf{e}_z \times (\mathbf{l}_{i-1,i} - \mathbf{l}_{i+1,i}) + (\Gamma P_C - \Lambda) (\hat{\mathbf{l}}_{i-1,i} + \hat{\mathbf{l}}_{i+1,i}) - \gamma \frac{1}{z_i} \mathbf{v}_i \right), \\ \hat{\boldsymbol{\sigma}}_C &= -\frac{p_C}{2A_C} \sum_{i \in C} \tilde{\mathbf{r}}_i \otimes [\mathbf{e}_z \times (\mathbf{l}_{i-1,i} - \mathbf{l}_{i+1,i})] - \frac{(\Gamma P_C - \Lambda)}{A_C} \sum_{i \in C} \tilde{\mathbf{r}}_i \otimes (\hat{\mathbf{l}}_{i-1,i} + \hat{\mathbf{l}}_{i+1,i}) - \frac{\gamma}{A_C} \sum_{i \in C} \frac{1}{z_i} \tilde{\mathbf{r}}_i \otimes \mathbf{v}_i. \end{aligned} \quad (\text{S13})$$

Now, let us compute the tensor $\tilde{\mathbf{r}}_i \otimes [\mathbf{e}_z \times (\mathbf{l}_{i-1,i} - \mathbf{l}_{i+1,i})]$. We first note that $\mathbf{l}_{i\pm 1,i} = \tilde{\mathbf{r}}_{i\pm 1} - \tilde{\mathbf{r}}_i$. Further,

$$\begin{aligned} [\tilde{\mathbf{r}}_i \otimes (\mathbf{e}_z \times (\mathbf{l}_{i-1,i} - \mathbf{l}_{i+1,i}))]_{\alpha\beta} &= \tilde{r}_{i,\alpha} [\mathbf{e}_z \times (\tilde{\mathbf{r}}_{i-1} - \tilde{\mathbf{r}}_{i+1})]_{\beta} \\ &= \tilde{r}_{i,\alpha} (\delta_{\beta,y} (\tilde{r}_{i-1,x} - \tilde{r}_{i+1,x}) - \delta_{\beta,x} (\tilde{r}_{i-1,y} - \tilde{r}_{i+1,y})). \end{aligned} \quad (\text{S14})$$

If we now multiply the last expression by $\frac{1}{2}$ and sum over all vertices, we obtain

$$\left[\frac{1}{2} \sum_{i \in C} \tilde{\mathbf{r}}_i \otimes (\mathbf{e}_z \times (\mathbf{l}_{i-1,i} - \mathbf{l}_{i+1,i})) \right]_{\alpha\beta} = A_C \delta_{\alpha\beta}. \quad (\text{S15})$$

We proceed to find $\tilde{\mathbf{r}}_i \otimes (\hat{\mathbf{l}}_{i-1,i} + \hat{\mathbf{l}}_{i+1,i})$. Since all these terms appear under a sum that is cyclic (i.e., over all vertices) we can shift indices as convenient to write,

$$\begin{aligned} \sum_{i \in C} \tilde{\mathbf{r}}_i \otimes (\hat{\mathbf{l}}_{i-1,i} + \hat{\mathbf{l}}_{i+1,i}) &= \sum_{i \in C} \left[\frac{\tilde{\mathbf{r}}_{i+1} \otimes (\tilde{\mathbf{r}}_i - \tilde{\mathbf{r}}_{i+1})}{|\tilde{\mathbf{r}}_i - \tilde{\mathbf{r}}_{i+1}|} + \frac{\tilde{\mathbf{r}}_i \otimes (\tilde{\mathbf{r}}_{i+1} - \tilde{\mathbf{r}}_i)}{|\tilde{\mathbf{r}}_{i+1} - \tilde{\mathbf{r}}_i|} \right] \\ &= \sum_{i \in C} \frac{(-\tilde{\mathbf{r}}_{i+1} + \tilde{\mathbf{r}}_i) \otimes (\tilde{\mathbf{r}}_{i+1} - \tilde{\mathbf{r}}_i)}{|\tilde{\mathbf{r}}_{i+1} - \tilde{\mathbf{r}}_i|} = - \sum_{i \in C} |\mathbf{l}_{i+1,i}| [\hat{\mathbf{l}}_{i+1,i} \otimes \hat{\mathbf{l}}_{i+1,i}]. \end{aligned} \quad (\text{S16})$$

This enables us to write the stress tensor for cell C as

$$\hat{\boldsymbol{\sigma}}_C = -p_C \hat{I} + \frac{(\Gamma P_C - \Lambda)}{A_C} \sum_{i \in C} |\mathbf{l}_{i+1,i}| \hat{\mathbf{l}}_{i+1,i} \otimes \hat{\mathbf{l}}_{i+1,i} - \frac{\gamma}{2A_C} \sum_{i \in C} \frac{1}{z_i} (\tilde{\mathbf{r}}_i \otimes \mathbf{v}_i + \mathbf{v}_i \otimes \tilde{\mathbf{r}}_i), \quad (\text{S17})$$

where we symmetrized the last viscous part. When calculating stresses according to the above Eq. (S17) we removed the affine part of the velocity field by replacing the vertex velocities \mathbf{v}_i with velocities $\mathbf{v}_i - \mathbf{v}_i^{\text{affine}}$, where the affine part of the velocity field is

$$\mathbf{v}_i^{\text{affine}} = \frac{d\hat{\mathbf{F}}}{dt} \mathbf{r}_i. \quad (\text{S18})$$

Here, $\hat{\mathbf{F}}$ is the deformation gradient due to the applied external deformation. For the oscillatory external deformation with the frequency ω_0 , the stress contribution due to the friction resulting from the affine part of the velocity field $\mathbf{v}_i^{\text{affine}}$ is linearly proportional to the driving frequency ω_0 and it dominates at large frequencies (see Fig. S3).

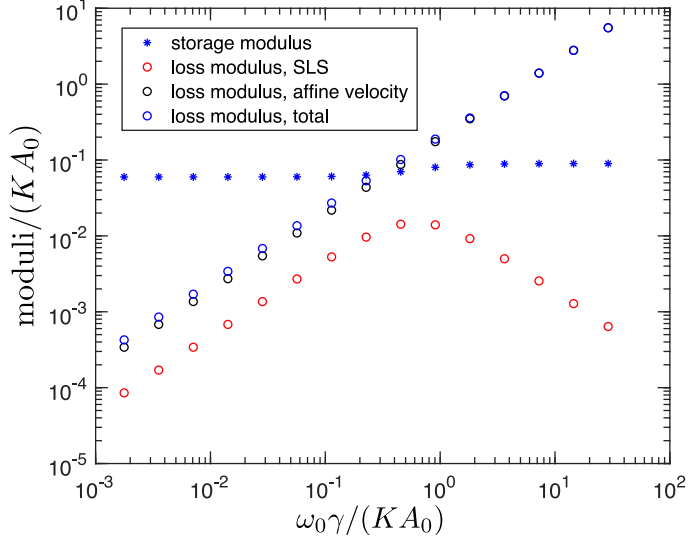


FIG. S3. The effect of the friction resulting from the affine velocity $\mathbf{v}_i^{\text{affine}}$ in Eq. (S18) on the loss shear modulus for $p_0 = 3.5$.

II. CONNECTION BETWEEN STRESS RESPONSE AND RHEOLOGY

Fig. S4 shows a typical average shear stress $\tau(t)$ in response to an applied oscillatory simple shear with the strain $\epsilon = \epsilon_0 \sin(\omega_0 t)$. The shear stress response can be represented as $\tau(t) = \tau_0 \sin(\omega_0 t + \delta) = \tau_0 \cos(\delta) \sin(\omega_0 t) + \tau_0 \sin(\delta) \cos(\omega_0 t)$. The storage shear modulus is related to the in-phase response and is defined as $G' = (\tau_0/\epsilon_0) \cos \delta$. The loss shear modulus is related to the out-of-phase response and is defined as $G'' = (\tau_0/\epsilon_0) \sin \delta$ [55].

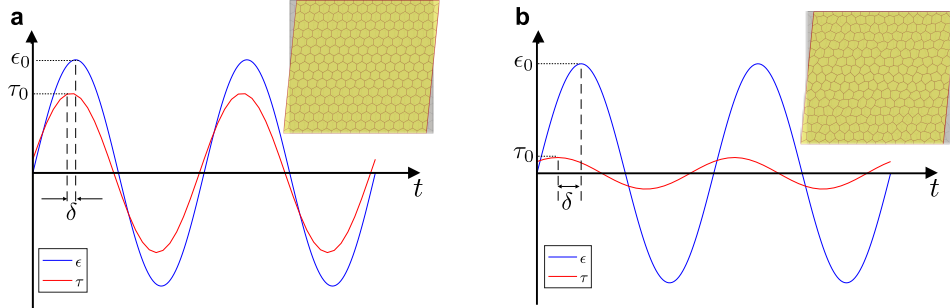


FIG. S4. Typical shear stress (red curve) as a function of time in response to a periodic shear strain (blue curve) in (a) the solid phase and (b) the fluid phase. The shear stress is averaged over all cells.

III. APPROACH OF THE RESPONSE STRESS TOWARDS THE STEADY STATE

Here, we show an example of how the steady state shear stress $\tilde{\tau}(\omega_0)$ is measured in response to the applied oscillatory simple shear with a time period $T_0 = 27.7\gamma/(KA_0) = 2\pi/\omega_0$ for the shape parameter $p_0 = 3.723$, which is very close to the critical point $p_c \approx 3.722$ for the solid-fluid transition. The shear stress signal $\tau(t)$ was divided into blocks of length $T = 3T_0$, each containing 3 cycles of the time period of the driving shear deformation (see Fig. S5a). Within each block n , we performed the Fourier transform of $\tau(t)$ and obtained $\tilde{\tau}_n(\omega)$ as

$$\tilde{\tau}_n(\omega) = \frac{1}{T} \int_{(n-1)T}^{nT} \tau(t) e^{i\omega t} dt, \quad (S19)$$

where n is a positive integer. The value of $\tilde{\tau}_n(\omega_0)$ converges exponentially to the steady state value (see Fig. S5b), where the relaxation time is related to the characteristic time scales of the viscoelastic models (see Fig. 2c,d in the main text). For values of p_0 far away from p_c , the system quickly reaches a steady state (within 3–6 cycles). As p_0 approaches p_c the relaxation times become much longer, which is reflecting the diverging characteristic time scales of the viscoelastic models (see Fig. 2c,d in the main text).

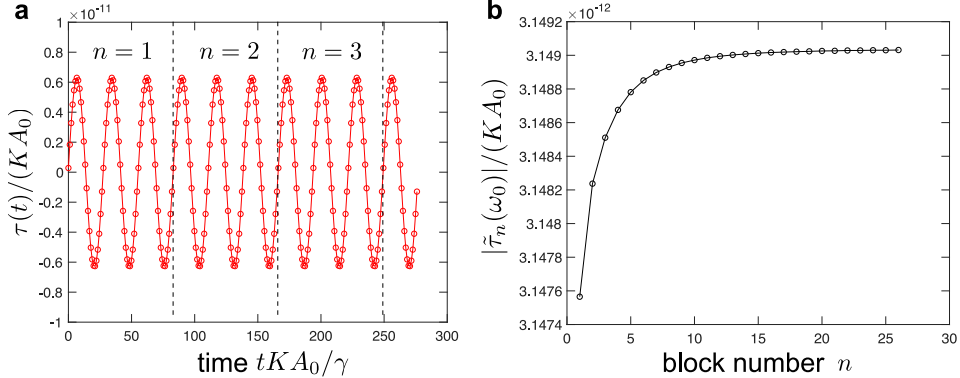


FIG. S5. Approach of the response shear stress towards the steady state. (a) The shear stress signal $\tau(t)$ was divided into blocks indicated by the vertical dashed lines. (b) Fourier transform of the response shear stress $\tilde{\tau}_n(\omega_0)$ at the driving frequency, ω_0 , as a function of the block number, n .

IV. RESIDUAL HYDROSTATIC STRESS IN THE SOLID PHASE

In the solid phase, we studied the rheology of the hexagonal lattice with each cell of area $A_C = A_0$ but with the perimeter P_C not equal to the preferred perimeter P_0 , which induces residual hydrostatic stress in equilibrium. This residual stress can be eliminated if the lattice is uniformly rescaled by a factor α , which minimizes the following dimensionless energy per cell,

$$e_C(\alpha) = \frac{1}{2} (\alpha^2 - 1)^2 + \frac{\tilde{\Gamma}}{2} (\alpha p_C - p_0)^2, \quad (\text{S20})$$

where $e_C = \frac{E_C}{KA_0^2}$, $\tilde{\Gamma} = \frac{\Gamma}{KA_0}$, $p_C = \frac{P_C}{\sqrt{A_0}} = \sqrt[4]{192} \approx 3.722$, i.e., α is a root of $e'_C(\alpha) = 0$. In the solid phase, $\alpha < 1$, and the system shrinks to relax the residual stress if it is not held by the periodic boundary conditions. At the solid-fluid transition point, $\alpha = 1$ since the area and perimeter of each cell match their preferred values simultaneously. If the residual stress is eliminated by rescaling the box, the rheology of the system subject to a simple shear can still be described by the SLS model, although the fitted values of spring constants are different, as shown in Fig. S6.

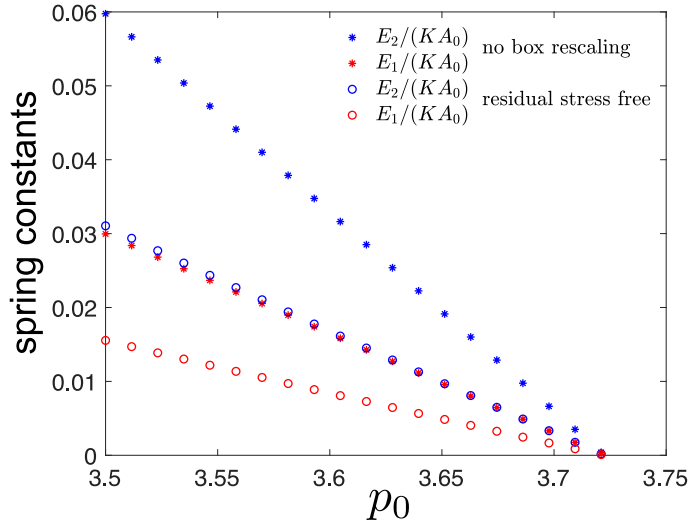


FIG. S6. The fitted spring constants in the solid phase when the simulation box is not rescaled (closed symbols) and rescaled (open symbols) to eliminate residual stresses.

V. COLLAPSE OF STORAGE AND LOSS SHEAR MODULI IN THE FLUID PHASE

In Fig. 1f in the main text, we showed the collapse of storage and loss shear moduli for the fluid phase in the low frequency regime. Here we show the collapse in the high frequency range (see Fig. S7), where we took into account that the relevant characteristic timescale scales as $\eta_2/E_2 \sim \gamma/(KA_0)$.

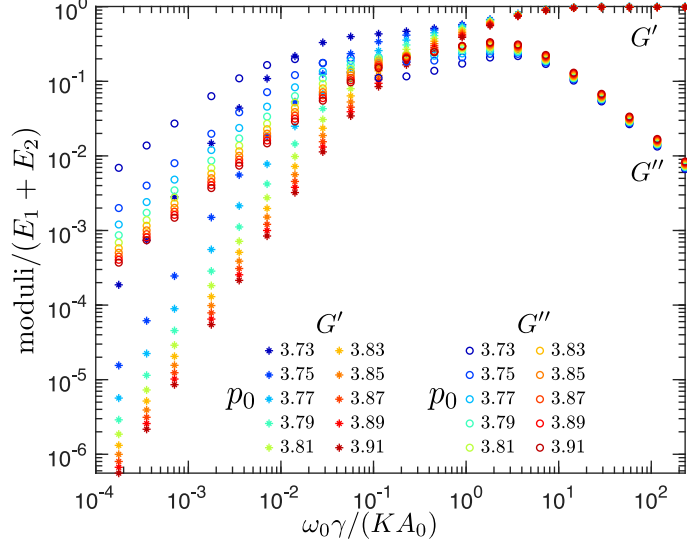


FIG. S7. The collapse of the storage (G') and loss (G'') shear moduli curves in the high frequency regime for different values of p_0 for the fluid phase.

VI. EFFECTS OF THE INITIAL PERTURBATION IN THE FLUID PHASE

We note that the rheological behavior in the fluid phase is sensitive to the magnitude σ_D of the initial perturbation that was used to obtain different local energy minima configurations. In the main text, we showed the fitted values of spring and dashpot constants (Fig. 2) for the local energy minima configurations that were obtained by displacing each vertex coordinate of the hexagonal tiling by a Gaussian random variable with zero mean and standard deviation $\sigma_D = 1.5 \times 10^{-4} \sqrt{A_0}$. Here, we show that the fitted values of the spring and dashpot constants are somewhat sensitive to the magnitude σ_D of the random perturbation (see Fig. S8).

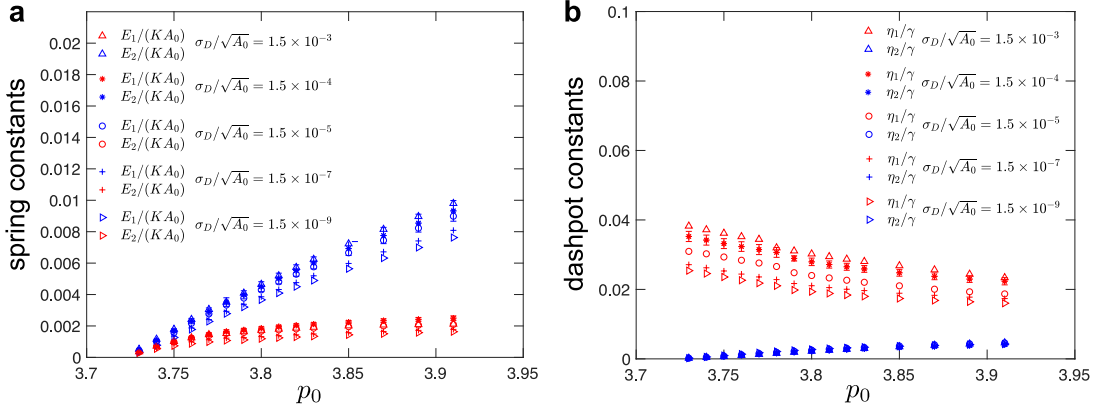


FIG. S8. Fitted values of (a) spring and (b) dashpot constants for the system under simple shear deformation as a function of the target cell-shape parameter, p_0 , and the magnitude σ_D of the random perturbation that was used to obtain different local energy minima configurations in the fluid phase. Errorbars correspond to the standard deviation for simulations that were repeated for configurations that correspond to different local energy minima.

VII. TUNING PHASE TRANSITION WITH DIFFERENT MODES OF DEFORMATION.

In the main text, we showed that the solid-fluid transition point can be tuned by uniaxially pre-compressing/stretching the system. Here we discuss other deformation modes that can also tune the transition. If the hexagonal lattice is deformed biaxially by $\hat{\mathbf{F}} = \begin{pmatrix} a & 0 \\ 0 & a \end{pmatrix}$, the shear modulus due to the affine deformation becomes

$$G_{\text{affine}} = 3\sqrt{3}\Gamma \left(1 - \frac{p_0}{ap_c} \right). \quad (\text{S21})$$

By setting G_{affine} to 0, the phase boundary in the $a - p_0$ plane is

$$a(p_0) = \frac{p_0}{p_c}. \quad (\text{S22})$$

Similarly, consider a pure shear deformation $\hat{\mathbf{F}} = \begin{pmatrix} a & 0 \\ 0 & 1/a \end{pmatrix}$. The shear modulus due to the affine deformation then becomes

$$G_{\text{affine}} = \frac{2\sqrt{2} (1 + \sqrt{1 + 3a^4} + 3a^4\sqrt{1 + 3a^4}) (2\sqrt{2} 3^{1/4}(1 + \sqrt{1 + 3a^4}) - 3ap_0) \Gamma}{3^{7/4}a(1 + 3a^4)^{3/2}}, \quad (\text{S23})$$

and the phase boundary is

$$p_0(a) = \frac{2\sqrt{2} 3^{1/4}(1 + \sqrt{1 + 3a^4})}{3a}. \quad (\text{S24})$$

The phase diagrams for a system that is under biaxial deformation or pure shear are shown in Fig. S9. The phase boundary in $a - p_0$ plane follows Eq. (S22) for biaxial deformation and Eq. (S24) for pure shear. The system can be rigidified by stretching or shearing.

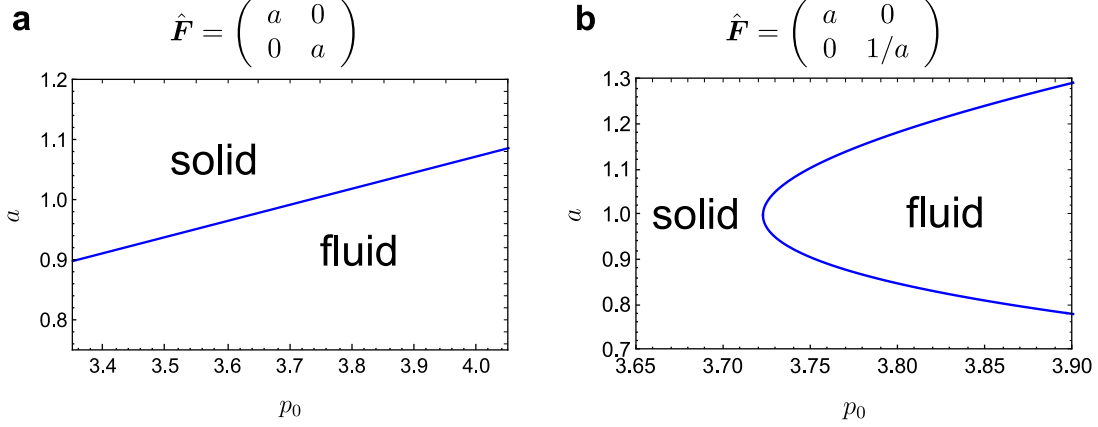


FIG. S9. Phase diagrams when the system is under (a) biaxial deformation and (b) pure shear.

Note that there are two equivalent ways of derive the shear modulus due to affine deformation. The first one is to calculate the energy density of the system perturbed by an additional simple shear $\hat{\mathbf{F}} = \begin{pmatrix} 1 & \epsilon \\ 0 & 1 \end{pmatrix}$ where $\epsilon \ll 1$. For example, for the hexagonal tiling without any pre-deformation (i.e., regular hexagons), the energy density can be expanded in a power series in ϵ as

$$\frac{E}{A_0} = \frac{1}{2}3\sqrt{3} \left(1 - \frac{p_0}{p_c} \right) \Gamma \epsilon^2 + o(\epsilon^4) \equiv \frac{1}{2}G_{\text{affine}}\epsilon^2 + o(\epsilon^4), \quad (\text{S25})$$

where $p_c = 2\sqrt{2} 3^{1/4} \approx 3.722$ and we neglected the constant term. The quadratic term characterizes the linear response of the system, which gives the shear modulus as in Eq. (5) in the main text. The second approach is to directly use the elastic part of the stress formula Eq. (S17) by setting the velocity \mathbf{v}_i to be 0. Assume the system is perturbed by a simple shear $\hat{\mathbf{F}} = \begin{pmatrix} 1 & \epsilon \\ 0 & 1 \end{pmatrix}$ where $\epsilon \ll 1$, and calculate the shear stress. The coefficient of the leading order term in ϵ is the shear modulus, which coincides with the modulus from the energy calculation. Similar derivation of the shear modulus can be carried out for the pre-deformed hexagonal tilings.

VIII. SPECTRUM OF THE NORMAL MODES

We calculated the eigenvalues λ of the Hessian matrix associated with the energy functional of the VM. We associate each positive eigenvalue λ with a corresponding eigenfrequency $\omega = \sqrt{\lambda}$, which describes the oscillations of that mode as the system is perturbed about its stable point. Fig. S10 shows the cumulative density of states, which is defined as

$$N(\omega) = \int_{0+}^{\infty} D(\omega') d\omega' + N(\lambda = 0)\theta(\omega), \quad (\text{S26})$$

where $D(\omega)$ is density of states, $N(\lambda = 0)$ is the fraction of zero eigenvalues and $\theta(\omega)$ is the Heaviside step function. In the solid phase, there are no zero modes other than the two translational rigid body motions. In the fluid phase, however, approximately half of the eigenmodes are zero modes. As p_0 approaches the critical value p_c in both solid and fluid phase, $N(\omega)$ curves move to the left so the system becomes softer, which is consistent with the dependence of the spring constants on p_0 shown in Fig. 2a in the main text.

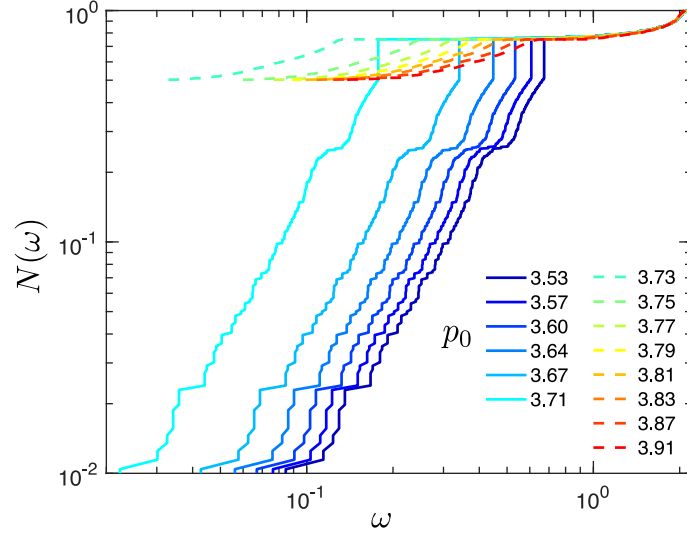


FIG. S10. Cumulative density of states in the solid phase (solid lines) and in the fluid phase (dashed lines).